actuators

MDPI

Article

Modeling and Hysteresis Inverse Compensation Control of Soft Pneumatic Gripper for Gripping Phosphorites

Yang Zhang [1], Junjie Lu [2], Zixin Huang [2,3,4] and Bing Feng [1,*]

[1] College of Management, Wuhan Institute of Technology, Wuhan 430205, China; zhangyang@wit.edu.cn
[2] School of Electrical and Information Engineering, Wuhan Institute of Technology, Wuhan 430205, China; lujunjie_2002@163.com (J.L.); huangzx@wit.edu.cn (Z.H.)
[3] Yunnan Key Laboratory of Unmanned Autonomous Systems, Yunnan Minzu University, Kunming 650504, China
[4] Provincial Engineering Research Center for New Energy Vehicle Intelligent Control and Simulation Test Technology of Sichuan, Xihua University, Chengdu 610039, China
* Correspondence: fengbing@wit.edu.cn

Abstract: The emergence of soft robots provides new opportunities for developing phosphorite processing equipment. In this article, a soft pneumatic gripper (SPG) for gripping phosphorites is designed. On this basis, the dynamic modeling method and hysteresis inverse compensation control method for the SPG are proposed. First, an SPG for gripping phosphorites is designed based on pneumatic actuation technology. Meanwhile, the gripping ability of the designed SPG is experimentally examined. Next, a dynamic model of the SPG is established by combining the Bouc–Wen model and a linear dynamic model. The output of the established dynamic model can fit the experimental data well, which shows that the established dynamic model of the SPG can describe its motion characteristics. Then, by constructing the inverse expression of the established dynamic model, the hysteresis inverse compensation control method for the SPG is presented to realize its motion control. Finally, the result of the control system simulation illustrates that the presented control method is effective.

Keywords: soft pneumatic gripper (SPG); dynamic modeling; Bouc–Wen model; hysteresis inverse compensation

check for updates

Academic Editor: Rocco Antonio Romeo

Received: 16 March 2025
Revised: 8 April 2025
Accepted: 13 April 2025
Published: 14 April 2025

Citation: Zhang, Y.; Lu, J.; Huang, Z.; Feng, B. Modeling and Hysteresis Inverse Compensation Control of Soft Pneumatic Gripper for Gripping Phosphorites. *Actuators* **2025**, *14*, 193. https://doi.org/10.3390/act14040193

Copyright: © 2025 by the authors. Licensee MDPI, Basel, Switzerland. This article is an open access article distributed under the terms and conditions of the Creative Commons Attribution (CC BY) license (https://creativecommons.org/licenses/by/4.0/).

1. Introduction

In the production process of the phosphorite industry, the selection of minerals has a significant impact on both the quality and the efficiency of production [1]. The quality of minerals directly relates to the overall quality of the products, while production efficiency directly affects the operational efficiency of the production line and cost control. Therefore, phosphorite companies strive to continually improve the accuracy and efficiency of selection processes by introducing advanced automated assembly equipment and processes, optimizing production workflows, and reducing human errors, ensuring smooth and efficient mineral selection processes [2]. Such ongoing efforts contribute to raising the quality level of minerals while simultaneously lowering production costs and enhancing the competitiveness of enterprises.

Soft robots are mainly made of soft material, and their actuators are also soft [3]. With the developments of soft material technologies and robotic technologies, soft robots are becoming a research hotspot [4]. Some fascinating soft robots have been developed, such as soft grippers [5], soft fish [6], and soft flapper vehicles [7]. The nature of softness gives

soft robots the ability to safely interact with humans. Therefore, soft robots have wide applications in the fields of wearable devices and health care.

According to the soft actuation technologies, soft robots can be divided into soft pneumatic robots [8], soft hydraulic robots [9], and soft smart material-based robots [10]. Soft smart material-based robots can be further classified as soft electric robots [7], soft optical robots [11], soft thermal robots [12], soft magnetic robots [13], and so on. The application of soft smart materials provides many promising functions for soft robots. However, soft smart materials have expensive costs and complex characteristics, bringing huge technical problems to the applications of smart material-based soft robots.

Besides the smart material-based soft robots, soft hydraulic robots are also expensive. Moreover, soft hydraulic robots require high sealing performance [14], which makes their fabrication difficult. From the aspects of cost, fabrication, lifetime, and reliability, soft pneumatic robots are currently closer to real-world applications. Researchers have achieved certain research results in soft pneumatic robots. In [15], a bubble-casting soft robot is developed, which can deform under the actuation of compressed air. In [16], a leopard-like soft robot is manufactured based on the pneumatic soft actuation technology, which can rapidly jump forward on a plane. In [17], a turtle-like soft pneumatic is developed, which can adapt to multi-environment locomotion. For gripping objects, soft pneumatic grippers (SPGs) are developed. In [18], an SPG based on the pneumatic bellow actuator is fabricated. In [19], a soft pneumatic hand is fabricated. Overall, the studies on SPGs are just beginning. The mechanical design, characteristic analysis, modeling, and control of the SPGs are facing great difficulties, providing researchers with a large number of research topics. In addition, there is a gap between SPGs and their practical applications in gripping phosphorites.

SPGs have great research value and application potential in gripping phosphorites and can be used to perform mineral beneficiation in a safe and efficient way. However, the design and manufacturing of the SPG confront difficulties. In addition, the modeling and control problems of the SPG should be addressed to facilitate its large-scale practical application. Considering that the soft pneumatic actuator (SPA) is the key component of the SPG, the modeling and control of the SPA must first be realized. However, the SPA has complicated hysteretic characteristics, which pose great difficulties in its modeling [20]. For SPA modeling, researchers usually analyze its physical principles to establish the model or use various phenomenological models to fit the input–output relationship directly. In [20], based on the Ogden model, a finite element analysis model of the SPA is established. In [21], a physical dynamic model of the SPA is established by studying its load dynamics, force dynamics, flow dynamics, and pressure dynamics. However, these two modeling processes are complicated.

Some phenomenological models are also used in the modeling of the SPA. In [22], a modified Bouc–Wen model is employed to establish the dynamic model of the SPA to describe its hysteretic characteristic. In [23], the hysteretic characteristic of the SPA is modeled based on the Prandtl–Ishlinskii model. However, using the above phenomenological hysteretic models alone cannot describe the creep characteristic of the SPA. Seeking a simple and comprehensive modeling method for the SPA is a key prerequisite for the implementing applications of the SPG.

Based on the above considerations, this study proposes the design, modeling, and control methods of the SPG used for gripping phosphorites. First, the SPG is designed and manufactured using soft pneumatic actuation technology and integrated injection molding technology, which possess gripping capacity for phosphorites. Then, two SPG experimental testbenches (experimental testbench A and experimental testbench B) are built. Next, using experimental testbench A, a series of gripping experiments of the SPG are conducted to exhibit its gripping ability. Moreover, using experimental testbench B and

applying the compressed air to the SPA, its characteristics are observed through an actuation experiment. After that, a dynamic model of the SPG is established by combining the Bouc–Wen model and a linear dynamic model. Finally, based on the established dynamic model, the hysteresis inverse compensation control method of the SPG is presented to realize its motion control. This research will significantly promote the application of SPGs in engineering practice.

The rest of this paper is organized as follows. Section 2 introduces the fundamentals of the SPG, and builds two experimental testbenches. Section 3 conducts some gripping experiments of the SPG. Section 4 studies the characteristics of the SPA and establishes its dynamic model. Section 5 presents the hysteresis inverse compensation control method of the SPG. Finally, Section 6 provides the conclusions.

2. Structural Design and Manufacturing of SPG

In this section, we first design a novel SPA and further conduct the structural design of the SPG. Then, two actual SPAs are manufactured, and they are employed to fabricate a whole SPG prototype.

2.1. Design of SPA

In this subsection, the structural design of the SPA is conducted. The 3D drawing of the SPA and its dimensions (unit: mm) are shown in Figure 1. It is obvious to see that the main body of the SPA has the dimensions of 100 mm × 18 mm × 20 mm. The SPA has six internally connected cavities. The local enlarged sectional view of the SPA is also provided in Figure 1. In the local enlarged sectional view, the design details and dimensions of the cavity are clearly exhibited.

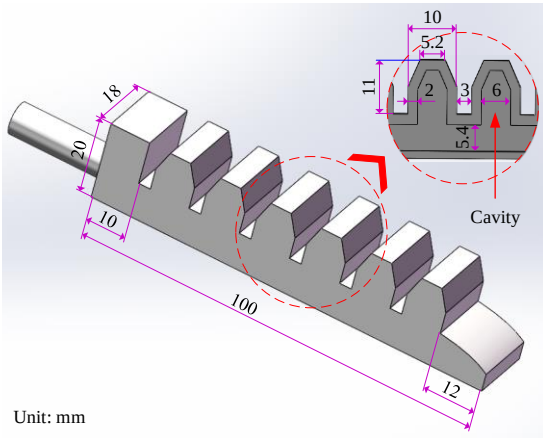

Figure 1. A 3D drawing of the SPA.

To provide a better exhibition of the SPA and illustrate its motion mechanism, its global sectional view is shown in Figure 2. Figure 2 clearly shows that the SPA consists of the air supply port, cavity, silicone layer, and confining layer. The SPA is deformed under the action of compressed air, the motion mechanism of which is illustrated below. When injecting the compressed air into the cavities of the SPA through its air supply port. The silicone layer produces deformation under the action of the compressed air, causing the cavities to gradually expand with the pressure of the increased compressed air. Meanwhile, compared with the silicone layer, the deformation ratio of the confining layer is small. On the basis of this situation, the deformation of the SPA on the side of the confining layer is confined, while its deformation on the side of the cavity is large. Thus, the SPA will bend towards the side of the confining layer (see Figure 2).

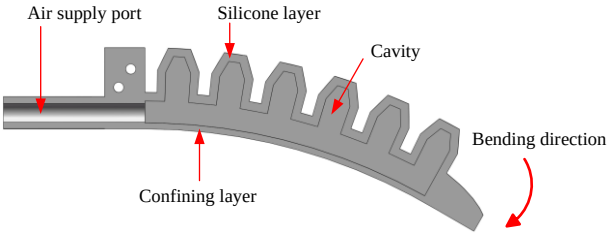

Figure 2. Global sectional view of SPA.

2.2. Design of SPG

In this subsection, the mechanical design of the SPG is conducted. The 3D assembly drawing of the SPG is shown in Figure 3. As shown in Figure 3, the SPG mainly consists of two SPAs (i.e., SPA1 and SPA2) and a base plate. These two SPAs are assembled symmetrically on the base plate.

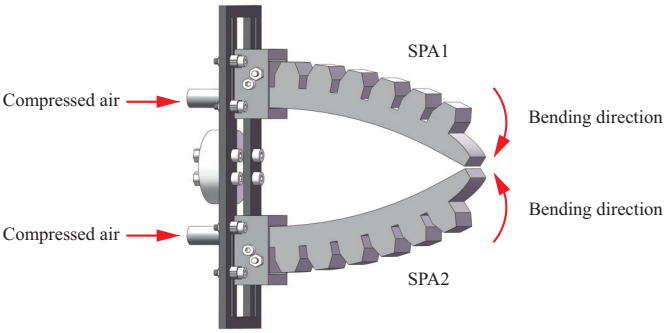

Figure 3. Motion diagram of SPG.

The work principle of the SPG is described as follows. According to the motion mechanism of the SPA, both SPA1 and SPA2 will produce a bending motion when compressed air is injected into SPA1 and SPA2 simultaneously. The bending directions of these two SPAs are annotated in Figure 3. As a result, SPA1 and SPA2 bend towards each other, leading to the end of SPA1 and the end of SPA2 approaching each other. This motion makes it possible to grip phosphates by using the SPG. When the pressure of the compressed air decreases, SPA1 and SPA2 will gradually restore to their initial state. During this motion process, the phosphates gripped by SPG will be released. By regulating the air pressure injected into SPA1 and SPA2, it is possible to use the SPG to grip and release phosphates. In other words, we can employ the SPG to conduct the beneficiation work of phosphates.

To manufacture the SPG, two SPAs are manufactured using the integrated injection molding technology first. The actual SPA is shown in Figure 4. Then, we use two actual SPAs and a base plate to manufacture the SPG. An actual SPG prototype shown in Figure 5 is manufactured, which is assembled by a based plate and two SPAs (i.e., SPA1 and SPA2).



Figure 4. Actual SPA.

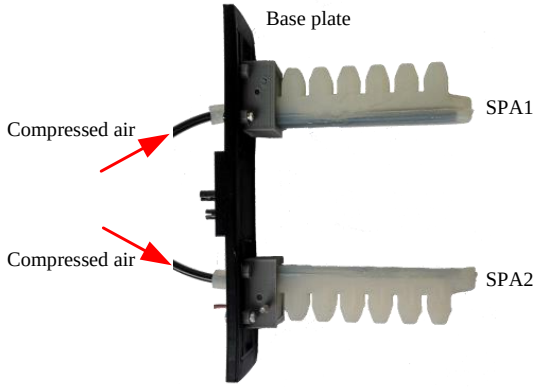

Figure 5. Actual SPG.

2.3. Experimental Testbench A

To test the gripping performance of the SPG, experimental testbench A is built. As shown in Figure 6, experimental testbench A mainly consists of a power supply module, a computer, a pump, a pressure regulation valve, a manipulator, and the manufactured SPG. The SPG is installed on the manipulator. The manipulator is employed to move the SPG to a certain position. Then, the gripping experiments of the SPG can be conducted.

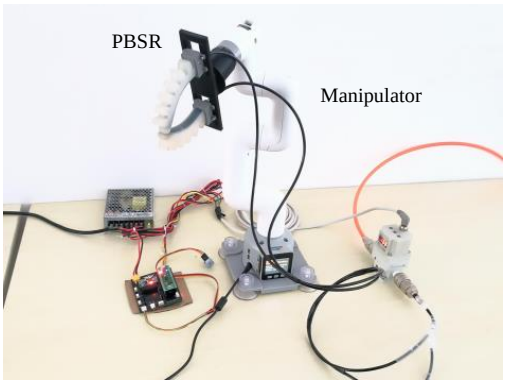

Figure 6. Experimental testbench A.

2.4. Experimental Testbench B

To investigate the characteristics of the manufactured SPA of the actual SPG prototype, experimental testbench B is built. As shown in Figure 7, experimental testbench B mainly includes a power supply module, a computer, a pump, a pressure regulation valve, an I/O board, a displacement sensor, and the manufactured SPA. The local enlarged sectional view in Figure 7 clearly shows the SPA fixed in experimental testbench B. Figure 7b shows the reference point, measuring point, and displacement y of the SPA. Specifically, the reference point is located at the lower plane of the SPA. The line connecting the reference point and the displacement sensor forms a one-dimensional coordinate system, where the vertical downward direction is the positive direction of the Y-axis, and the reference point is the coordinate origin. The measuring point is the intersection point between the Y-axis and the lower plane of the SPA. The coordinate position of the SPA's measuring point in the Y-axis is defined as its displacement y.

The power supply module will power the pressure regulation valve. The powers of other devices are supplied by a laboratory power supply with an amplitude of 220 V and a frequency of 50 Hz. The computer is used to control and monitor the actions of the whole system, including the pneumatic pressure signal production and data collection. The pump is used to provide the compressed air for the SPA. The pressure regulation valve is used to regulate the pneumatic pressure of the compressed air that is injected into the SPA. The

displacement sensor is used to measure the displacement of the SPA. The I/O board is used to send the pneumatic pressure signal to the pressure regulation valve and to receive the displacement signal measured by using the displacement sensor to the computer.

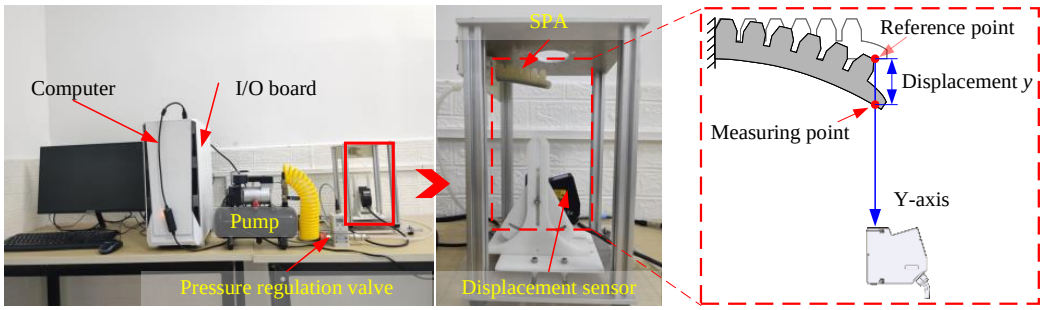

Figure 7. Experimental testbench B. (**a**) Pneumatic test platform and key components introduction. (**b**) Displacement measurement principle.

3. Gripping Experiments and Characteristic Analysis of SPG

In this section, the gripping performance of the SPG is experimentally tested using experimental testbench A.

To test the gripping ability of the SPG, we employ the SPG to grip some other parts with different shapes and dimensions. As shown in Figure 8, the screws, T-nut, stainless steel washer, and spiral spring can be successfully gripped. Therefore, the manufactured SPG can grip different parts, which indicates that the SPG has the potential to grip phosphorites.

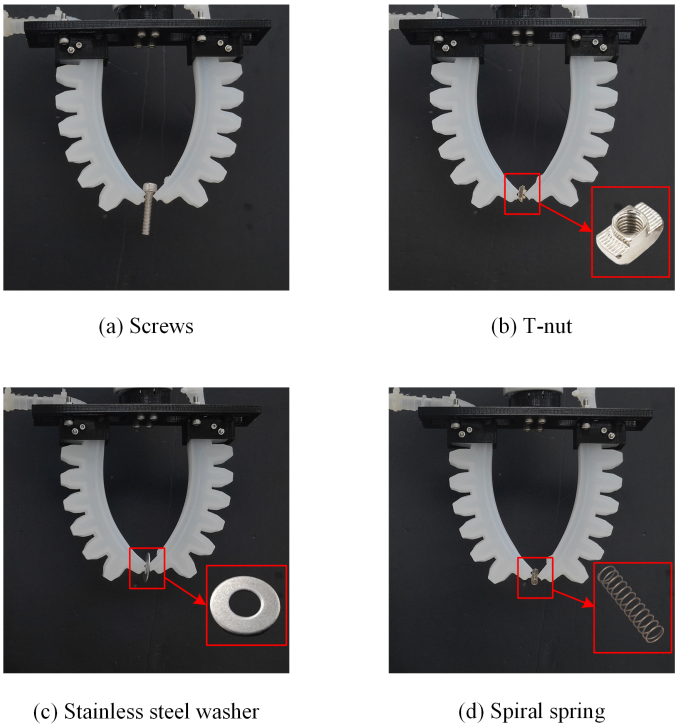

Figure 8. Different parts gripped by the SPG.

The irregular shapes, uneven sizes, and inconsistent weights of phosphorites make them challenging to grip. To address this problem, two SPAs of the manufactured SPG can envelope phosphorites to increase the contacted area to achieve the gripping objective of rocks (Figure 9). Compared to rigid grippers, the contact area when using the manufactured SPG is larger, which can ensure safe gripping for phosphorites. In addition, to the best of

our knowledge, there are currently few reports on the application research of existing soft grippers in gripping phosphorites. The manufactured SPG can grip phosphorites safely. Moreover, in the manufactured SPG, the confining layer that directly contacts phosphorites has a higher stiffness and wear resistance, which increases the bearing capacity of the SPG and prolongs its service life, facilitating the realization of practical applications.

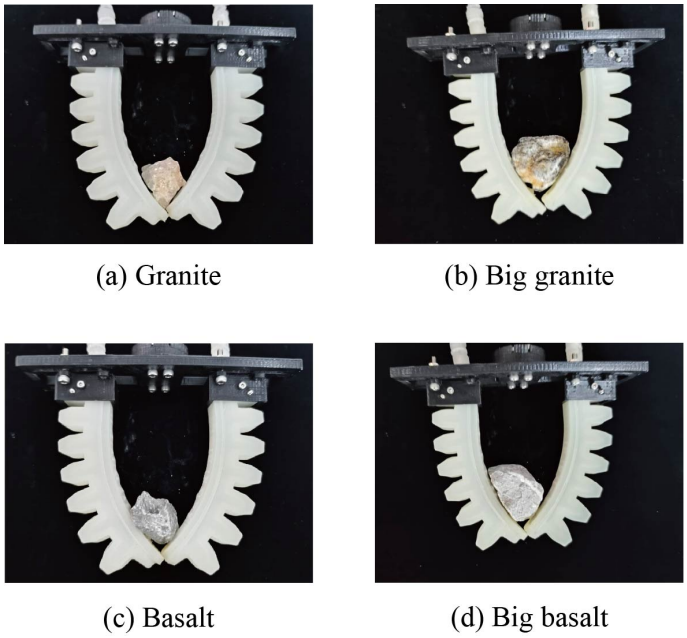

(a) Granite (b) Big granite

(c) Basalt (d) Big basalt

Figure 9. Different rocks gripped by the SPG.

4. Dynamic Modeling of SPA

To model the SPG, the main task is to establish a dynamic model of its SPA. In this section, the dynamic characteristics of the SPA are researched. Then, a dynamic model of the SPA is established to describe its characteristics under pneumatic actuation, which will provide a base for deeply researching and developing the recipes of the human acupoint treatment.

4.1. Dynamic Characteristics Analysis

To research the dynamic characteristics of the SPG under pneumatic actuation, a triangle pneumatic pressure with variable amplitudes and frequencies within one cycle is applied. This pressure is marked as TP1, and the amplitude of the pressure is denoted as p. Specifically, TP1 is shown as Figure 10a.

Under the actuation of TP1, the dynamic characteristics of the SPG's SPA are observed and analyzed according to the actual experimental results. The corresponding displacement y of the SPA in the Y-axis (see Figure 7) is shown in Figure 10b. Meanwhile, the corresponding hysteresis loops are shown in Figure 10c.

From Figure 10b,c, the dynamic characteristics of the SPG show complicated nonlinearities, which include the following:

- **Hysteresis characteristic:** The output displacement vs. input pressure curve forms the hysteresis loops. In addition, the shapes of the hysteresis loops are amplitude-dependent and frequency-dependent.
- **Creep characteristic:** The output displacement produces a drift along the application of the input pressure. In other words, the output displacement cannot return to its initial value when the input pressure backs to the initial value.

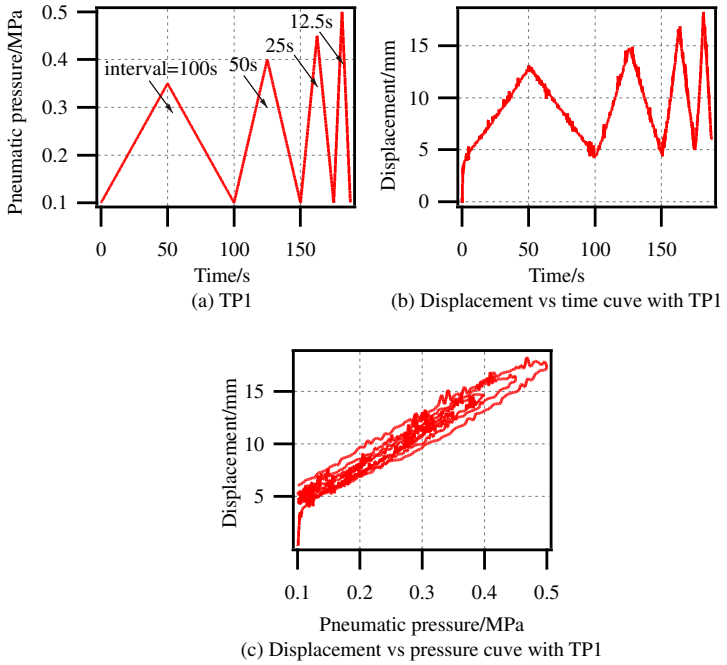

Figure 10. Input compressed air with cycle pneumatic pressure TP1 and corresponding characteristics.

4.2. Dynamic Model

The challenge of the dynamic modeling of the SPG lies in the modeling of its hysteresis characteristics and creep characteristics. For the hysteresis characteristic modeling, some hysteresis models such as the Jiles–Atherton model [24], Prandtl–Ishlinskii model [25], and Bouc–Wen model [26] have been developed. Compared with its counterparts, the Bouc–Wen model has the advantages of simpler mathematical expression and fewer parameters to be identified. More importantly, the Bouc–Wen model has a powerful capacity to describe the hysteresis characteristic. So, in this paper, the Bouc–Wen model is employed to establish the dynamic model of the SPG, which will also provide great benefits for its control.

According to [26], the Bouc–Wen model is expressed as

$$\begin{cases} B(t) = \alpha p(t) - h_{BW}(t) \\ \dot{h}_{BW} = \beta \dot{p} - \gamma \dot{p} |h_{BW}|^{\lambda} - \eta |\dot{p}| |h_{BW}|^{\lambda - 1} h_{BW} \end{cases} \tag{1}$$

where B is the output of the Bouc–Wen model and p is its input pneumatic pressure. h_{BW} is the hysteresis variable. λ is a positive integer. α, β, and γ are shape parameters of the hysteresis curves, which need to be identified.

According to (1), the block diagram of the Bouc–Wen model is shown in Figure 11.

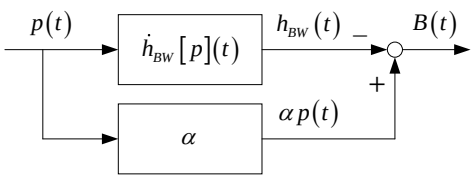

Figure 11. Block diagram of Bouc–Wen model.

Influenced by the viscoelasticity of the soft material, the SPG has complex viscoelastic characteristics. In addition, the hysteresis characteristic is contained by the dynamic viscoelastic characteristics. However, using the Bouc–Wen model alone can only describe the hysteresis characteristic of the SPG. So, a viscoelastic model of the SPG is established to

capture its creep characteristics and other dynamics viscoelastic characteristics. As shown in Figure 12, the viscoelastic model is established based on the generalized Kelvin–Voigt model that consists of several springs and dashpots. The stiffnesses of the springs are k_0, k_1, and k_2. The viscosity coefficients of the dashpots are c_1 and c_2. In addition, the viscoelastic model can be expressed as

$$\frac{V_E(s)}{p(s)} = \frac{1}{k_0} + \frac{1}{c_1 s + k_1} + \frac{1}{c_2 s + k_2} \tag{2}$$

where V_E is the output of the viscoelastic model, and s is the Laplace operator.

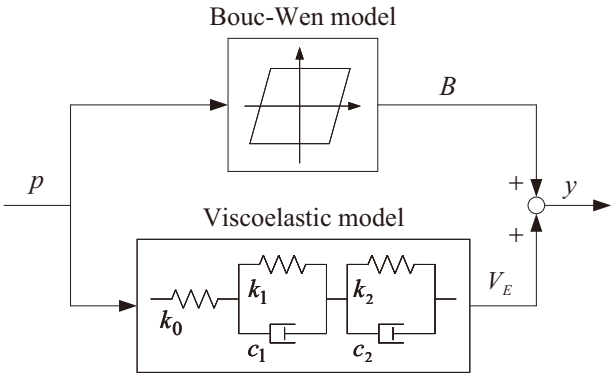

Figure 12. Block diagram of dynamic model of SPG.

By combining the Bouc–Wen model and the viscoelastic model, the dynamic model of the SPG is established, whose block diagram is shown in Figure 12. According to (1), (2), and Figure 12, the output of the dynamic model (i.e., the displacement of the SPG) can be expressed as (3). The established dynamic model of the SPG can describe its hysteresis characteristic and creep characteristic, and other dynamics viscoelastic characteristics.

$$y = B + V_E \tag{3}$$

where y is the displacement of the SPG.

4.3. Identification of Dynamic Model of SPG

In the previous section, the dynamic model of the SPG has been established. However, the parameters α, β, γ, λ, k_0, k_i, and c_i $(i = 1, 2)$ of the established dynamic model are unknown. In this subsection, these parameters are identified by using the *lsqcurvefit* function in MATLAB 2023a.

To execute the identification procedure, the compressed air with TP1 is applied to the SPG, and then the displacement data are collected. Based on the *lsqcurvefit* function in MATLAB, the values of TP1 and the collected displacement data, the unknown parameters α, β, γ, λ, n, k_0, k_i, and c_i $(i = 1, 2)$ are identified. Through the trial-and error-method, $\lambda = 1$ is presented. To quantitatively estimate the modeling accuracy, the following root-mean-squared error (RMSE) is used.

$$\begin{cases} e = y_c - y_m \\ e_{RMSE} = \sqrt{\dfrac{1}{N}\displaystyle\sum_{k=1}^{N} e_k^2} \end{cases} \tag{4}$$

where y_m is the output of the dynamic model of the SPG.

The identification results of other parameters are listed in (5). In the identification, the model output and the collected experimental displacement data are plotted and compared in Figure 13, the comparison of the corresponding hysteresis loops is shown in Figure 14, and the error plot is shown in Figure 15. Moreover, the RMSE is $e_{RMSE} = 0.194$ mm. It can be obtained from the above results that the established dynamic model of the SPG can describe its dynamic characteristics effectively.

$$\begin{cases} \alpha = 7.079, \beta = 17.207, \gamma = -2.093 \\ k_0 = 3.259, k_1 = 0.180, k_2 = 0.020 \\ c_1 = 2.461, c_2 = 0.012 \end{cases} \tag{5}$$

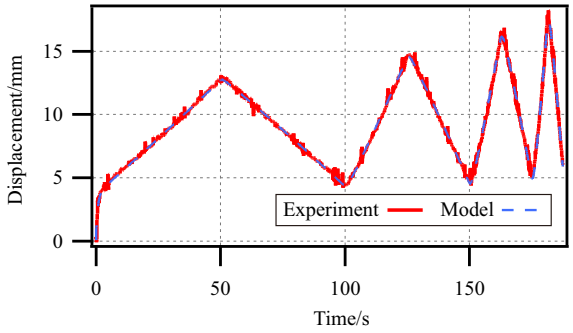

Figure 13. Comparison of the model output and the collected experimental displacement data.

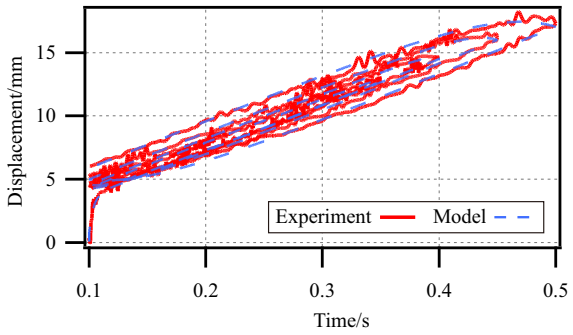

Figure 14. Comparison of hysteresis loops for the model output and the collected experimental displacement data.

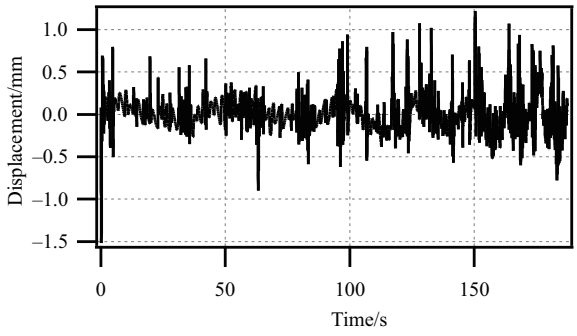

Figure 15. Error of the model output and the collected experimental displacement data in parameter identification.

According to (1) to (3) and the identification results of the parameters, the dynamic model of the SPG is expressed as

$$\begin{cases} B(t) = \alpha p(t) - h_{BW}(t) \\ \dot{h}_{BW} = \beta \dot{p} - \gamma \dot{p} |h_{BW}| - \eta |\dot{p}| |h_{BW}| h_{BW} \\ \dfrac{V_E(s)}{p(s)} = \dfrac{1}{k_0} + \dfrac{1}{c_1 s + k_1} + \dfrac{1}{c_2 s + k_2} \\ y = B + V_E \end{cases} \tag{6}$$

4.4. Validation of Dynamic Model of SPG

To validate the generalization of the established dynamic model of the SPG, the compressed air with TP2, SP1, and SP2 (Figure 16) is injected into its soft physiotherapy massage device. Meanwhile, by substituting TP2, SP1, and SP2 into the established dynamic model, the corresponding model outputs are computed.

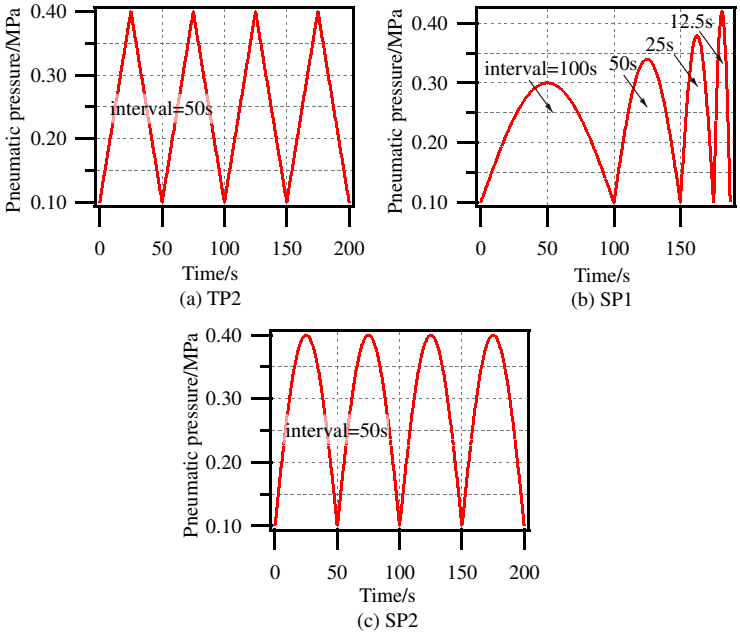

Figure 16. Compressed air input with cycle pneumatic pressure TP2, SP1, and SP2.

For the compressed air with TP2, the comparison of the model output and the collected displacement data are shown in Figure 17, the comparison of the hysteresis loops is shown in Figure 18, and the error plot is shown in Figure 19. According to Figures 17–19, the model output fits the collected displacement data well. In addition, the RMSE is $e_{RMSE} = 0.256$ mm.

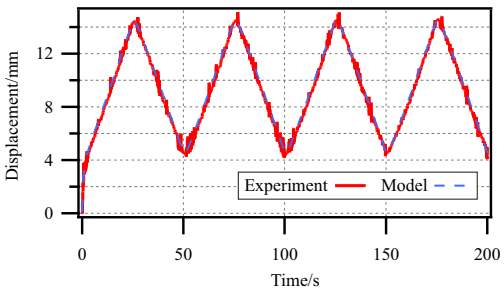

Figure 17. Comparison of the model output and the collected displacement data for the compressed air with TP2.

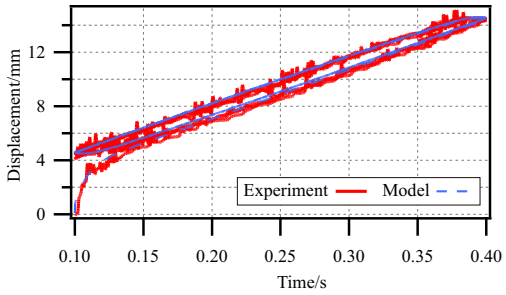

Figure 18. Comparison of the hysteresis loops of the model output and the collected displacement data for the compressed air with TP2.

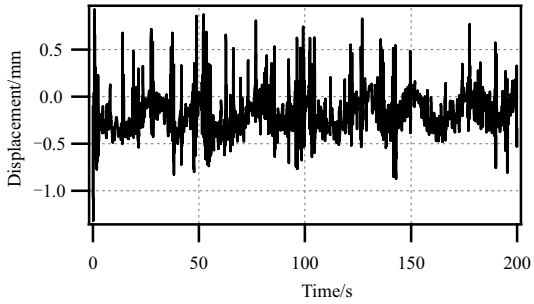

Figure 19. Error of the model output and the collected experimental displacement data with TP2.

For the compressed air with SP1, the comparison of the model output and the collected displacement data are shown in Figure 20, the comparison of the hysteresis loops is shown in Figure 21, and the error plot is shown in Figure 22. According to Figures 20–22, the model output can fit the collected displacement data well. In addition, the RMSE is $e_{RMSE} = 0.540$ mm.

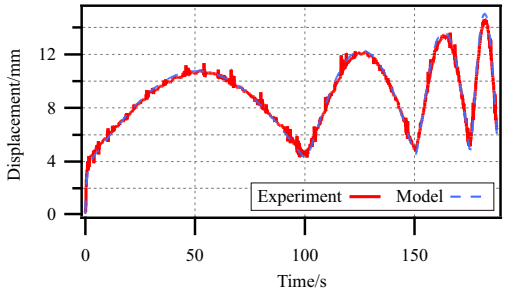

Figure 20. Comparison of the model output and the collected displacement data for the compressed air with SP1.

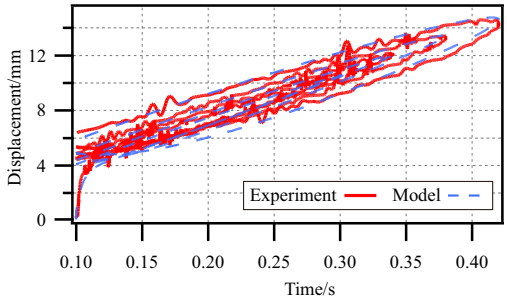

Figure 21. Comparison of the hysteresis loops of the model output and the collected displacement data for the compressed air with SP1.

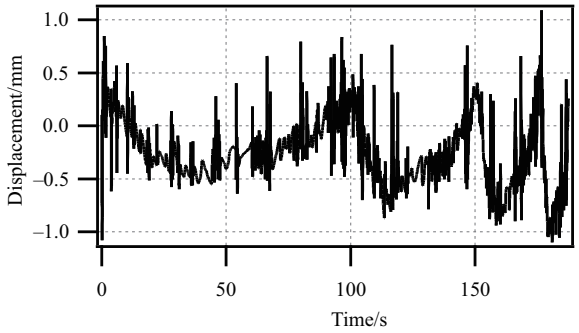

Figure 22. Error of the model output and the collected experimental displacement data with SP1.

For the compressed air with SP2, the comparison of the model output and the collected displacement data are shown in Figure 23, the comparison of the hysteresis loops is shown in Figure 24, and the error plot is shown in Figure 25. According to Figures 23–25, the model output can fit the collected displacement data well. In addition, the RMSE is $e_{RMSE} = 0.392$ mm.

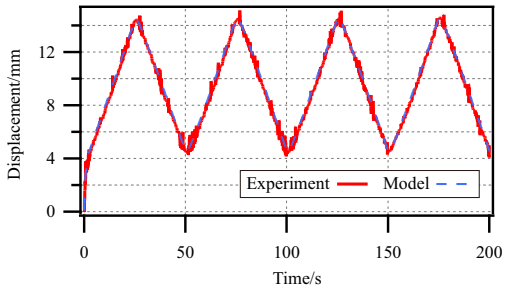

Figure 23. Comparison of the model output and the collected displacement data for the compressed air with SP2.

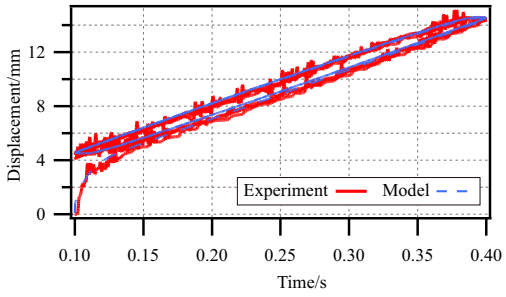

Figure 24. Comparison of the hysteresis loops of the model output and the collected displacement data for the compressed air with SP2.

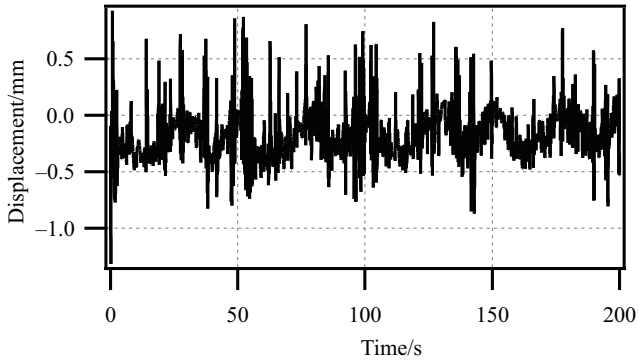

Figure 25. Error of the model output and the collected experimental displacement data with SP2.

According to the above model validation results, the output of the established dynamic model can fit the collected displacement data well, and the RMSE is not larger than $e_{RMSE} = 0.540$ mm. Therefore, the established dynamic model of the SPG has strong generalization.

Remark 1. *In addition to being suitable for the configuration of our SPA, the proposed modeling method can also be used in other variations of SPA. The reasons are listed below. (1) The SPAs are made of similar soft materials, leading to them having similar hysteresis characteristics and creep characteristics. (2) The proposed dynamic modeling method for the SPA is a data-driven phenomenological modeling method. Therefore, the dynamic model framework proposed in this paper can be extended to other variations of SPA. The only difference lies in the need to collect new experimental data on other variations of SPA for parameter identification.*

5. Hysteresis Inverse Compensation Control of the SPA

To realize the control of the SPA, a hysteresis inverse compensation controller is designed by constructing the Bouc—Wen model (see Figure 11). The designed hysteresis inverse compensation controller is used as the feedforward controller (see Figure 26) to compensate for the hysteresis characteristic of the SPA. By this means, the control of the SPA is transformed to design a PID feedback controller to realize the control of the linear system (i.e., the viscoelastic model shown in Figure 12). The diagram of the whole control system is shown in Figure 26. By combining the feedforward controller and PID feedback controller in parallel, a feedforward-feedback hybrid controller is designed to realize the control of the SPA.

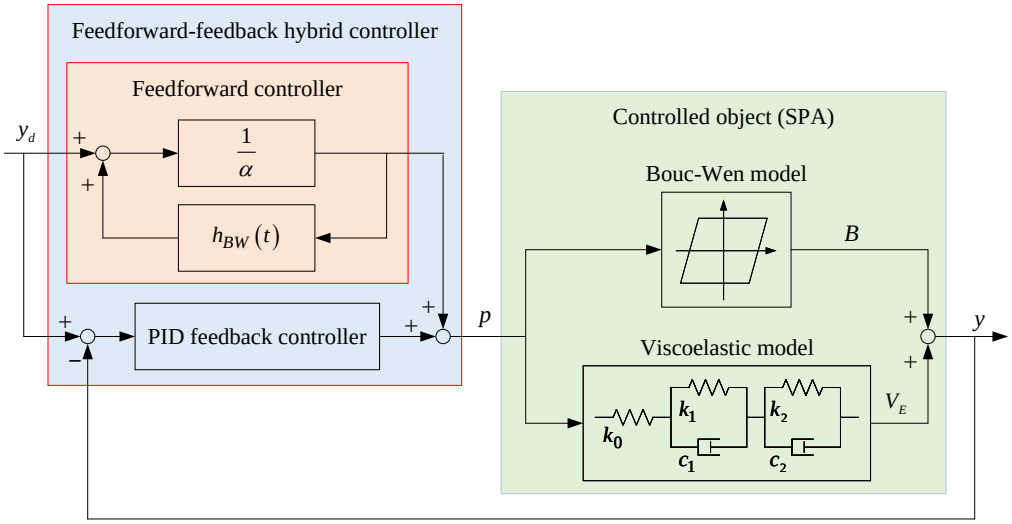

Figure 26. Control system of the SPA.

By using the presented feedforward-feedback hybrid controller, a simulation is conducted to verify the effectiveness of the proposed control method. In this simulation, the control object is the dynamic model of the SPA. The simulation result is shown in Figure 27. According to Figure 27, it can be seen that the simulation displacement of the SPA can track the desired displacement well, which indicates that the proposed feedforward-feedback hybrid control method is effective. In this future work, we will further verify the effectiveness of actual physical control experiments of the SPA.

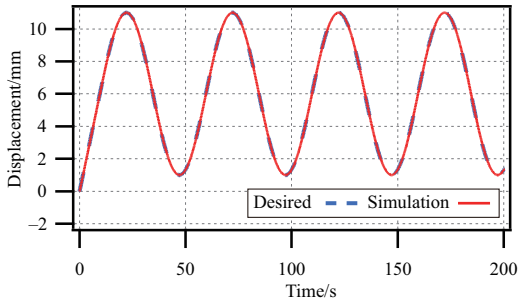

Figure 27. Comparison of the desired displacement and the simulation displacement of the SPA.

6. Conclusions

In this paper, the modeling and control methods of the SPG are presented. First, the SPG is designed and manufactured. Next, a series of gripping experiments of the SPG are conducted to exhibit its gripping ability. Gripping experimental results reveal that the gripping for phosphorites with irregular shapes, uneven sizes, and inconsistent weights is realized. Moreover, the hysteresis and creep characteristics of the SPA are observed through actuation experiments. After that, a dynamic model of the SPG is established by combining the Bouc–Wen model with a linear dynamic model. The results of the model identification and model validation show that the established dynamic model can effectively describe the abovementioned dynamic characteristics of the SPG, and RMSE is no more than 0.55 mm. Finally, based on the established dynamic model, the hysteresis inverse compensation control method of the SPG is presented to realize its motion control.

Compared to other modeling methods, the proposed method can not only simultaneously and accurately describe the hysteresis and creep characteristics of the SPG but also construct the inverse of the dynamic model, which facilitates the design of the hysteresis inverse compensation controller. Meanwhile, the proposed feedforward-feedback hybrid control method based on the hysteresis inverse compensation controller and PID feedback controller combines the advantages of feedforward and feedback control methods, which is beneficial for improving the control performance of the SPG.

The manufactured SPG has the properties of flexibility and safety, and its ability to grip phosphorites with irregular shapes, uneven sizes, and inconsistent weights has been validated experimentally. Since the current SPG is an original prototype, there are still some limitations that need to be addressed in future versions. First, the number of SPAs should increase to enhance the load-bearing capacity of the SPG. Second, the shapes and dimensions of the base plate should be modified to install the SPAs to expand the size range of objects that can be gripped. Then, the practical deployment of the SPG should be realized. In our future work, we will utilize the strong scalability of the SPAs and base plate to reconfigure the SPG with different numbers of the SPAs and different dimensions of the base plate to improve its load-bearing capacity and gripping size range further. In addition, we plan to deploy our SPG to an actual phosphorite stope to research its practical control and working performance, thus promoting its application in the engineering practice of the phosphorite industry.

Author Contributions: Conceptualization and writing—original draft, Y.Z.; formal analysis and writing—review and editing, J.L. and Z.H.; software, B.F.; investigation, Y.Z.; resources and writing—review and editing, B.F. All authors have read and agreed to the published version of the manuscript.

Funding: This research was funded by the Nature Science Foundation of Hubei Province (Grant No. 2023AFB380), the Foundation of Yunnan Key Laboratory of Unmanned Autonomous Systems (Grant

No. 202408YB06),the Foundation of Provincial Engineering Research Center for New Energy Vehicle Intelligent Control and Simulation Test Technology of Sichuan (Grant No. QCCK2024-0011).

Data Availability Statement: The original contributions presented in the study are included in the article. Further inquiries can be directed to the corresponding author.

Conflicts of Interest: The authors declare no conflicts of interest.

References

1. Jordens, A.; Cheng, Y.P.; Waters, K.E. A review of the beneficiation of rare earth element bearing minerals. *Miner. Eng.* **2013**, *41*, 97–114. [CrossRef]
2. Yang, X. Beneficiation studies of tungsten ores—A review. *Miner. Eng.* **2018**, *125*, 111–119. [CrossRef]
3. Rus, D.; Tolley, M.T. Design, fabrication and control of soft robots. *Nature* **2015**, *521*, 467–475. [CrossRef]
4. El-Atab, N.; Mishra, R.B.; Al-Modaf, F.; Joharji, L.; Alsharif, A.A.; Alamoudi, H.; Diaz, M.; Qaiser, N.; Hussain, M.M. Soft actuators for soft robotic applications: A review. *Adv. Intell. Syst.* **2020**, *2*, 2000128. [CrossRef]
5. Han, W.B.; Ko, G.J.; Lee, K.G.; Kim, D.; Lee, J.H.; Yang, S.M.; Kim, D.J.; Shin, J.W.; Jang, T.M.; Han, S.; et al. Ultra-stretchable and biodegradable elastomers for soft, transient electronics. *Nat. Commun.* **2023**, *14*, 2263. [CrossRef]
6. Li, G.R.; Chen, X.P.; Zhou, F.H.; Liang, Y.M.; Xiao, Y.H.; Cao, X.; Zhang, Z.; Zhang, M.Q.; Wu, B.S.; Yin, S.Y.; et al. Self-powered soft robot in the Mariana Trench. *Nature* **2021**, *591*, 66–71. [CrossRef]
7. Chen, Y.F.; Zhao, H.C.; Mao, J.; Chirarattananon, P.; Helbling, E.F.; Hyun, N.s.P.; Clarke, D.R.; Wood, R.J. Controlled flight of a microrobot powered by soft artificial muscles. *Nature* **2019**, *575*, 324–329. [CrossRef]
8. Xavier, M.S.; Tawk, C.D.; Zolfagharian, A.; Pinskier, J.; Howard, D.; Young, T.; Lai, J.; Harrison, S.M.; Yong, Y.K.; Bodaghi, M.; et al. Soft pneumatic actuators: A review of design, fabrication, modeling, sensing, control and applications. *IEEE Access* **2022**, *10*, 59442–59485. [CrossRef]
9. Yuk, H.; Lin, S.; Ma, C.; Takaffoli, M.; Fang, N.X.; Zhao, X. Hydraulic hydrogel actuators and robots optically and sonically camouflaged in water. *Nat. Commun.* **2017**, *8*, 14230. [CrossRef]
10. Shen, Z.; Chen, F.; Zhu, X.; Yong, K.T.; Gu, G. Stimuli-responsive functional materials for soft robotics. *J. Mater. Chem. B* **2020**, *8*, 8972–8991. [CrossRef]
11. Nocentini, S.; Parmeggiani, C.; Martella, D.; Wiersma, D.S. Optically driven soft micro robotics. *Adv. Opt. Mater.* **2018**, *6*, 1800207. [CrossRef]
12. Lendlein, A. Fabrication of reprogrammable shape-memory polymer actuators for robotics. *Sci. Robot.* **2018**, *3*, eaat9090. [CrossRef] [PubMed]
13. Hu, W.; Lum, G.Z.; Mastrangeli, M.; Sitti, M. Small-scale soft-bodied robot with multimodal locomotion. *Nature* **2018**, *554*, 81–85. [CrossRef] [PubMed]
14. Zatopa, A.; Walker, S.; Menguc, Y. Fully soft 3D-printed electroactive fluidic valve for soft hydraulic robots. *Soft Robot.* **2018**, *5*, 258–271. [CrossRef]
15. Jones, T.J.; Jambon-Puillet, E.; Marthelot, J.; Brun, P.T. Bubble casting soft robotics. *Nature* **2021**, *599*, 229–233. [CrossRef]
16. Tang, Y.; Chi, Y.; Sun, J.; Huang, T.H.; Maghsoudi, O.H.; Spence, A.; Zhao, J.; Su, H.; Yin, J. Leveraging elastic instabilities for amplified performance: Spine-inspired high-speed and high-force soft robots. *Sci. Adv.* **2020**, *6*, eaaz6912. [CrossRef]
17. Baines, R.; Patiballa, S.K.; Booth, J.; Ramirez, L.; Sipple, T.; Garcia, A.; Fish, F.; Kramer-Bottiglio, R. Multi-environment robotic transitions through adaptive morphogenesis. *Nature* **2022**, *610*, 283–289. [CrossRef]
18. Gai, L.J.; Huang, J.; Zong, X. Stiffness-Tunable Soft Bellows Actuators by Cross-Fiber Jamming Effect for Robust Grasping. *IEEE/ASME Trans. Mechatronics* **2023**, *28*, 2897–2907. [CrossRef]
19. Terryn, S.; Brancart, J.; Lefeber, D.; Assche, G.V.; Vanderborght, B. Self-healing soft pneumatic robots. *Sci. Robot.* **2017**, *2*, eaan4268. [CrossRef]
20. Moseley, P.; Florez, J.M.; Sonar, H.A.; Agarwal, G.; Curtin, W.; Paik, J. Modeling, design, and development of soft pneumatic actuators with finite element method. *Adv. Eng. Mater.* **2016**, *18*, 978–988. [CrossRef]
21. Shen, X. Nonlinear model-based control of pneumatic artificial muscle servo systems. *Control Eng. Pract.* **2010**, *18*, 311–317. [CrossRef]
22. Dao, Q.T.; Le, H.T.; Nguyen, M.L.; Do, T.H.; Duong, M.D. A Modified Bouc-Wen Model of Pneumatic Artificial Muscles in Antagonistic Configuration. In Proceedings of the 2020 International Conference on Advanced Mechatronic Systems, Hanoi, Vietnam, 10–13 December 2020; pp. 157–161.
23. Xie, S.; Ren, G.; Wang, B. A modified asymmetric generalized Prandtl–Ishlinskii model for characterizing the irregular asymmetric hysteresis of self-made pneumatic muscle actuators. *Mech. Mach. Theory* **2020**, *149*, 103836. [CrossRef]
24. Annakkage, U.; McLaren, P.; Dirks, E.; Jayasinghe, R.; Parker, A. A current transformer model based on the Jiles-Atherton theory of ferromagnetic hysteresis. *IEEE Trans. Power Deliv.* **2000**, *15*, 57–61. [CrossRef]

25. Al Janaideh, M.; Rakheja, S.; Su, C.Y. An analytical generalized Prandtl–Ishlinskii model inversion for hysteresis compensation in micropositioning control. *IEEE/ASME Trans. Mechatronics* **2010**, *16*, 734–744. [CrossRef]
26. Ismail, M.; Ikhouane, F.; Rodellar, J. The hysteresis Bouc-Wen model, a survey. *Arch. Comput. Methods Eng.* **2009**, *16*, 161–188. [CrossRef]

Disclaimer/Publisher's Note: The statements, opinions and data contained in all publications are solely those of the individual author(s) and contributor(s) and not of MDPI and/or the editor(s). MDPI and/or the editor(s) disclaim responsibility for any injury to people or property resulting from any ideas, methods, instructions or products referred to in the content.